Zakharov, D.O., Zozulya, D.R., and Colòn, D.P., 2023, Quantitative record of the Neoarchean water cycle from a 2.67 Ga magmatic-hydrothermal system, Fennoscandian Shield: Geology, https://doi.org/10.1130/G50702.1

Zakharov et al., GSA GEOLOGY 2023: Supplemental Material

Quantitative Record of the Neoarchean Water Cycle from a 2.67 Ga Magmatic-Hydrothermal System, Fennoscandian Shield

David O. Zakharov[1,2], D.R. Zozulya[3], and D.P. Colòn[4]

[1]*Institute of Earth Sciences, University of Lausanne, Lausanne, Switzerland, CH-1015*

[2]*Department of Geological and Environmental Sciences, Western Michigan University, Kalamazoo, MI 49008, USA*

[3]*Geological Institute, Kola Science Centre of the Russian Academy of Sciences, Apatity, 184209, Russia*

[4]*Department of Earth Sciences, University of Geneva, Geneva, Switzerland CH-1205*

Supplemental Material

Sample Description

Peralkaline granites

Typical unaltered peralkaline granite is massive with a porphyritic structure, with large (1.5–2.0 cm) subhedral phenocrysts of microcline-perthite (40 vol%) and a fine- to medium-grained groundmass composed of equal amounts of xenomorphic albite, quartz, microcline, and aggregates of arfvedsonite and aegirine (±aenigmatite, astrophyllite). The peralkaline granites are leucocratic; the amount of mafic minerals does not exceed 7–8 vol. %. The porphyritic granite is typical of the White Tundra locality (locality #1 marked on **Fig. 1** Main Text; sample WT1-3). Other samples used here (locality #4; Ponoj granite, sample

PM8) shows a gneissic structure with linear-planar distribution of mafic minerals. The typical varieties of the peralkaline granites are shown below (see **Fig. S1**).

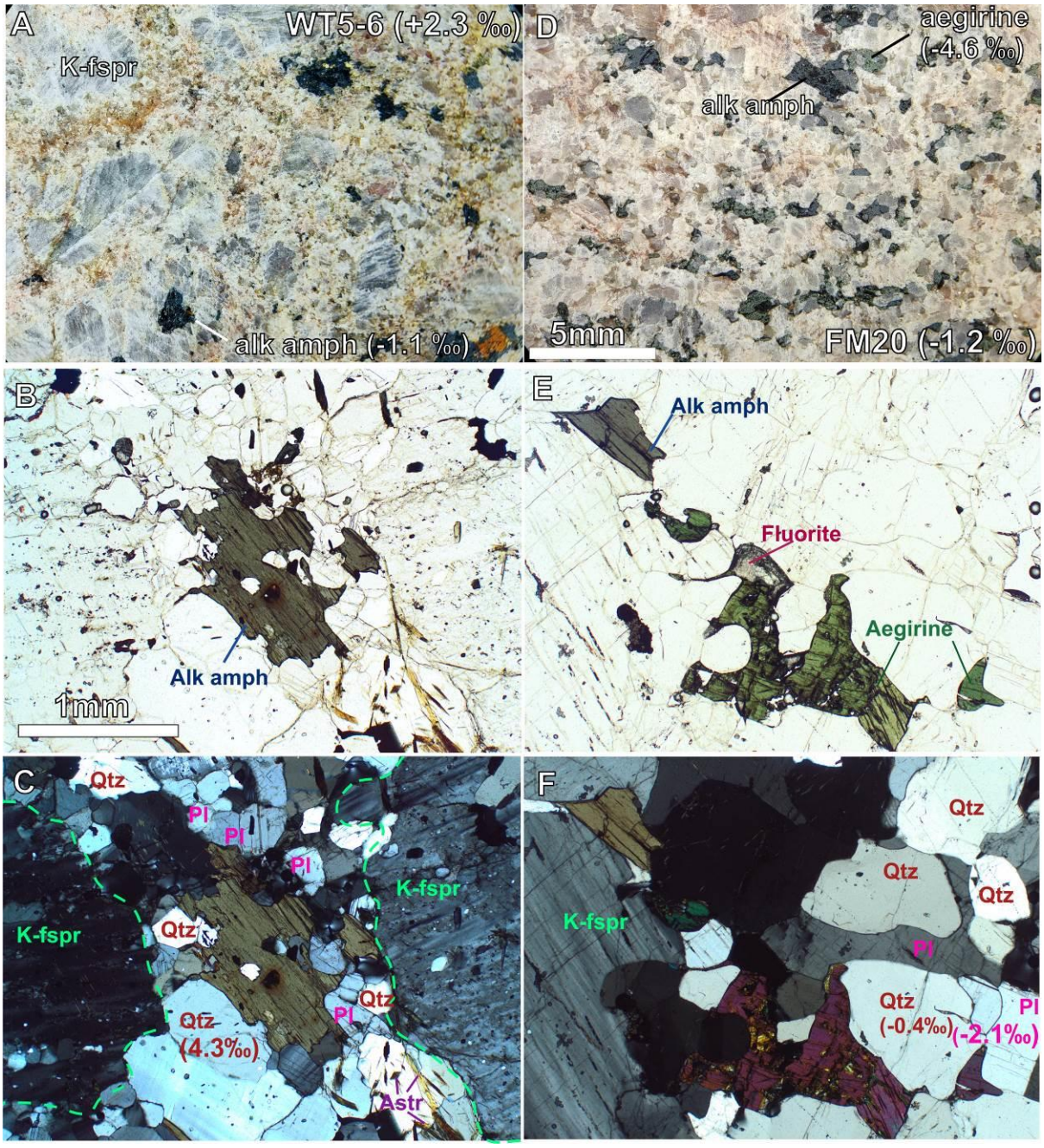

Figure S1. Varieties of peralkaline granites from the low $\delta^{18}O$ Keivy complex. Panels **A** though **C** depict the sample WT5-6 as seen in a hand sample (**A**), in cross polarized light with one nicol (**B**) and with crossed nicols (**C**). The rock exhibits a clear porphyritic texture with perthitic K-feldspar phenocrysts (outlined with bright green in **B**). Panels **D** - **F** depict a gneissic peralkaline granite with linear distribution of alkaline amphibole (arfvedsonite) and

aegirine. The abbreviations used in the figure: Alk amph = alkaline amphibole (arfvedsonite), K-fspr = K-feldspar, Qtz = quartz, Pl = plagioclase. The numbers in ‰ show the $\delta^{18}O$ values of mineral separates extracted from these samples (see **Fig. S5**).

Host rocks

Host rock samples are from metavolcanic Lebyazhka Formation. They are fine-grained garnet- and muscovite-bearing biotite gneisses which have massive and foliated structure in hand specimens (see **Fig. S2**). Typical gneiss contains relics of subeuhedral plagioclase and subordinate microcline phenocrysts up to 5 mm long, rare quartz phenocrysts up to 2.5 mm long, immersed into groundmass of fine-grained plagioclase (60-70 vol. %), quartz (10-20 vol. %), K-feldspar (5-10 vol. %), biotite (up to 5 vol. %). Based on these textural and geochemical features, garnet- and muscovite-bearing biotite gneiss can be interpreted as a metamorphosed porphyric trachyrhyolite (Balagansky et al., 2021). In proximity to the peralkaline granite intrusions, Lebyazhka gneisses are altered (see **Fig. S2**). Alteration includes formation of randomly oriented amphibole (ferrohastingsite) grains, and of chain-like aggregates of fluorite and newly crystallized K-feldspar (amazonite). Abundance of ferrohastingsite depends on the intensity of alteration and may reach 10 vol. %. Alteration amounts to several tens to hundreds of meters of thickness in the Lebyazhka Formation (Batieva, 1976).

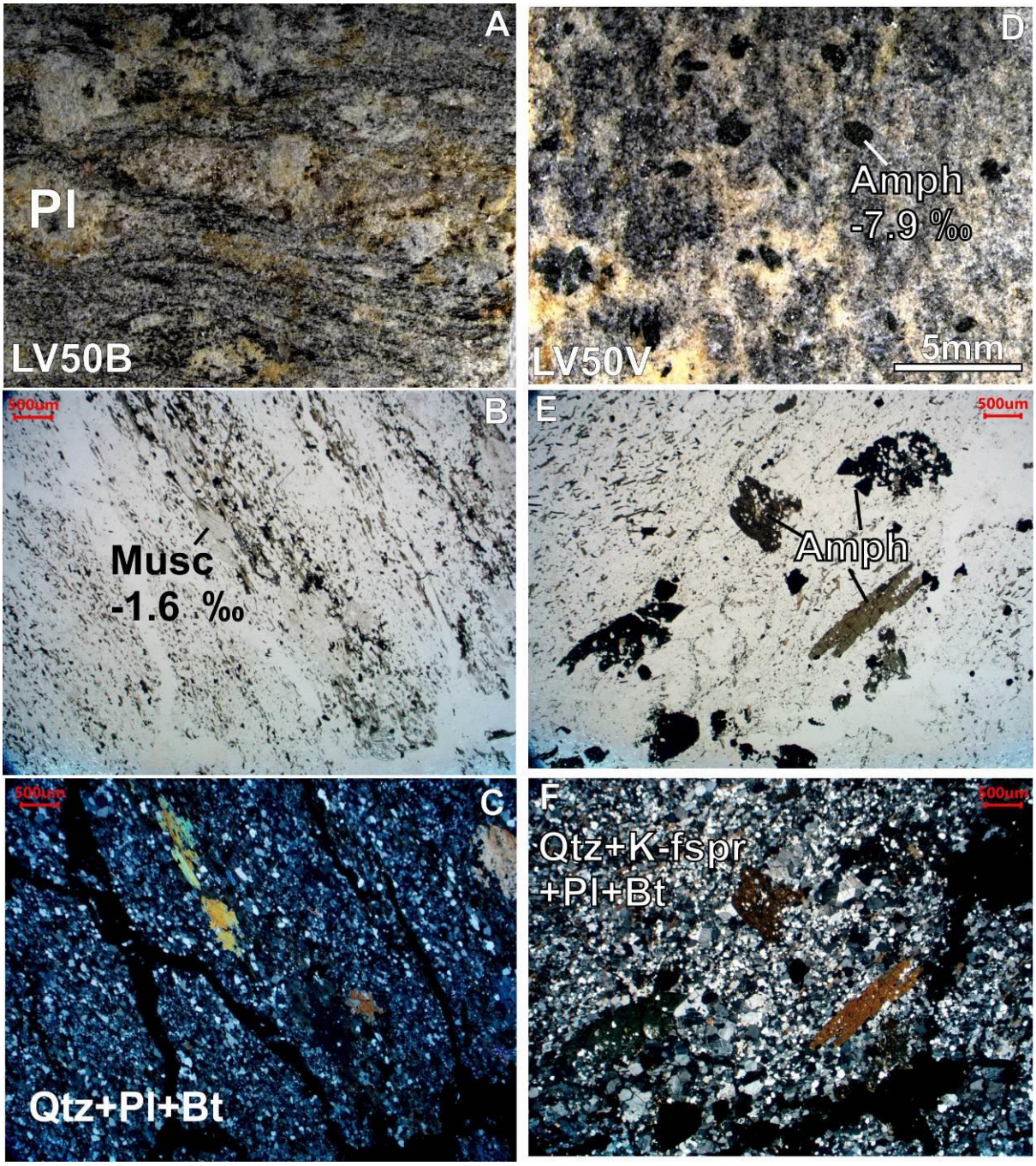

Figure S2. Photographs of host rocks. Panels **A** – **C** depict the sample of Lebyazhka Formation (sample LB50B) as seen in a hand sample (**A**), in cross polarized light with one nicol (**B**) and with crossed nicols (**C**). The mineralogical composition of the sample is similar to pristine unaltered host rock (garnet-muscovite-biotite gneiss). Panels **D** through **F** depict a sample of altered host rock from Lebyazhka Formation (LV50V). The alteration is notably expressed in the large porphyroblasts of amphibole and appearance of abundant K-feldspar

(microcline) in the matrix. The abbreviations used in the figure are the same as in **Fig. S1** with the following addition: musc = muscovite, bt = biotite.

Quartzolites

Quartzolites studied here are from Rova occurrence located in the apical parts of the peralkaline granites of the West Keivy (locality 2 on Fig. 1 Main Text). Quartzolites form irregularly shaped bodies varying from 0.5 to 1.5 m across and are hosted in the granites and the country rocks (samples PB161, PB177, PZ10). They are composed of quartz and mafic minerals, ranging in grain size from medium-grained to pegmatitic (see **Fig. S3**). Quartz contents range from 50 to 90 vol%. A distinguishing feature is the very low content of alkali feldspars (K-feldspar and albite compose <10 vol%). The primary mafic minerals are aegirine and arfvedsonite. Magnetite, ilmenite, annite and fluorite frequently occur in these quartzolites. Parts of the quartzolites are enriched in rare-metal (Zr, Y, REE, Nb, Ta) minerals reaching up to 20‑30 vol. %. Zircon (see **Fig. S3**) is a typical mineral for the rare-metal assemblages. Other rare-metal minerals are irregularly distributed and include aeschynite-(Y), chevkinite-(Ce), fergusonite-(Y), britholite-group minerals, yttrialite-(Y), thorite, monazite-(Ce), xenotime-(Y) and bastnäsite-(Ce). The irregular shape of the quartzolites within the peralkaline granites and host rocks as well as significant amounts of hydrous minerals, fluorite, and other F-bearing minerals (e.g., bastnäsite and britholite) point to the active involvement of hydrothermal fluids in the formation of the quartzolites. Thus, quartzolites probably formed as a product of focused fluid cycling in the apical parts of peralkaline granites and their host rocks.

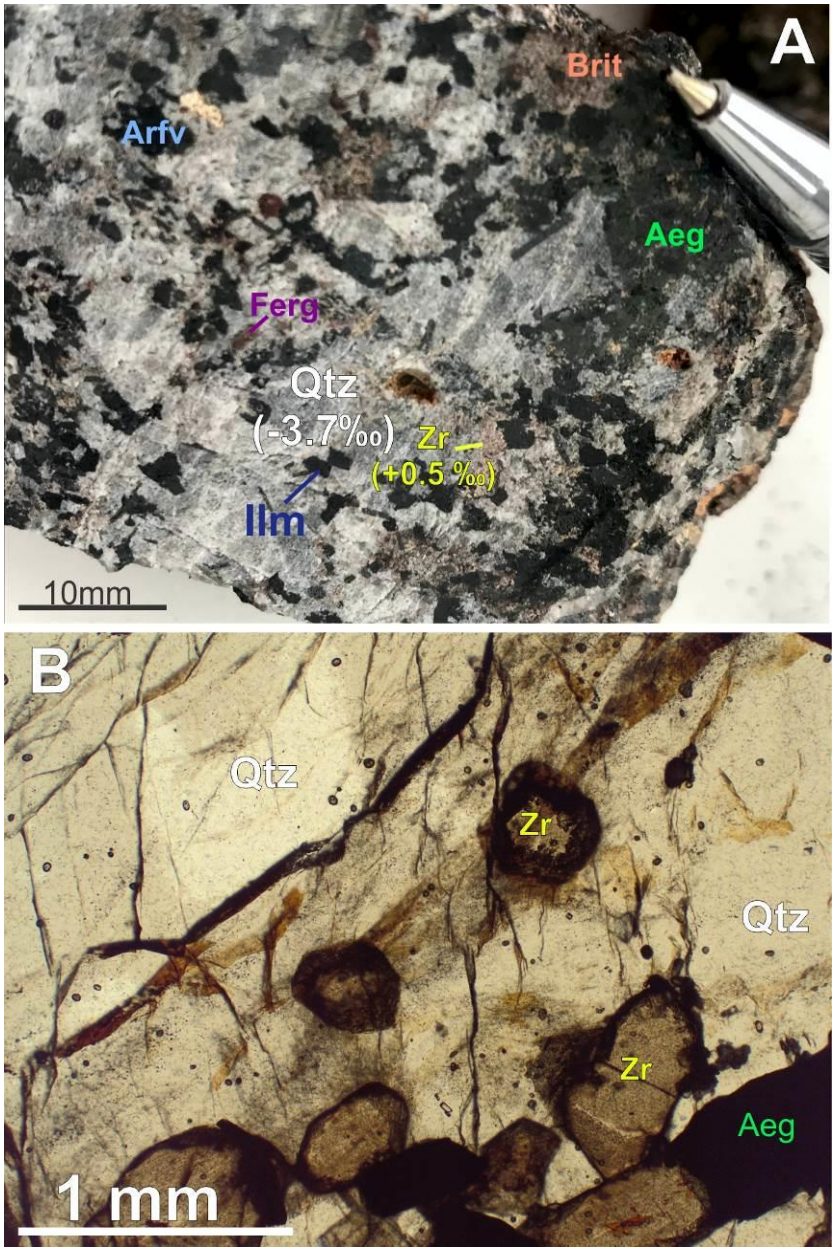

Figure S3. A – The sample of quartzolite (PB161) with the following minerals labeled: Aeg = aegirine, Arfv = arfvedsonite, Brit = britholite, Ferg = fergusonite, Ilm = ilmenite, Qtz = quartz, Zr = zircon. The $\delta^{18}O$ values are shown in parenthesis as measured by bulk laser fluorination technique. **B** – a thick section (100μm thick) of a quartzolite vein (sample FM20) showing quartz matrix and included grains of zircon and other minerals.

Methods

In situ $\delta^{18}O$ zircon measurements by SIMS

The $\delta^{18}O$ values of zircons extracted from the peralkaline granite samples PM8, WT1-3, PB161, PB177 and PZ10 were determined in situ using the Cameca IMS 1270 secondary ion mass spectrometer equipped with a cesium ion source installed at the CRPG-CNRS in Nancy, France. The zircon crystals were mounted in indium together with zircon standard 91500 ($\delta^{18}O$ = 9.9 ± 0.1 ‰; Wiedenbeck et al., 2004). Grains of secondary standard Penglai zircon ($\delta^{18}O$ = 5.3 ± 0.1 ‰; Li et al., 2010) were also mounted to monitor the accuracy of determinations. Prior to mounting in indium, the grains of unknows were polished in epoxy resin to expose the grain centers. These polished grains then were carefully extracted from the resin using a soldering iron. The crystals were studied under a Scanning Electron Microscope (SEM) CamScan MV2300 to acquire back-scattered electron (BSE) and cathodoluminescent (CL) images. Prior to analyses, the carefully washed, dried in an oven (60 °C), outgassed under vacuum and coated with a 35 nm layer of gold. During the analyses, the liquid nitrogen trap was used to obtain the best possible vacuum. The analyses employed a 10 kV Cs^+ primary ion beam with a ~2 nA current focused on a ~10 μm diameter spot. Pre-sputtering of targeted areas during 45 s was applied with a 10 μm raster before each measurement. The secondary ions were extracted using negative 10 kV potential applied to the sample holder. The $^{18}O/^{16}O$ ratios were measured using the mass resolving power of ~2400 in a multi-collection mode using two off-axis L'2 and H1 Faraday cup (FC) detectors. The obtained ion intensities of ^{16}O and ^{18}O were around 1.3×10^9 and 2.7×10^6 counts per second (cps), respectively. Additionally, we monitored the presence of water-containing domains in the analyzed zircons using the $^{16}OH/^{16}O$ ratio. Concurrently with the $^{18}O/^{16}O$ ratio, the $^{16}OH^-$ was measured on the axial FC2 detector using the mass resolving power of 5000 to separate the interference from ^{17}O. Each measurement consisted of 30 cycles with counting time of 5 s per cycle. Several measurements of the 91500 standards were made in

the beginning and the end of the session to monitor stability and accuracy of the analyses. Blocks of 4-5 unknowns were bracketed by 2-3 measurements of the 91500 zircon standard.

The instrumental uncertainty of $\delta^{18}O$ measurements is typically around 0.2 ‰. The typical reproducibility of 91500 zircon within each session (May and September 2021) is 0.3-0.5 ‰ (2 s.d.; n = 77). The analytical error of $^{16}OH/^{16}O$ signals is typically around 0.2-3 % relative to the mean. The variability of $^{16}OH/^{16}O$ during measurement cycles is depicted on **Fig. S4**. All the SIMS data is reported in Table S1.

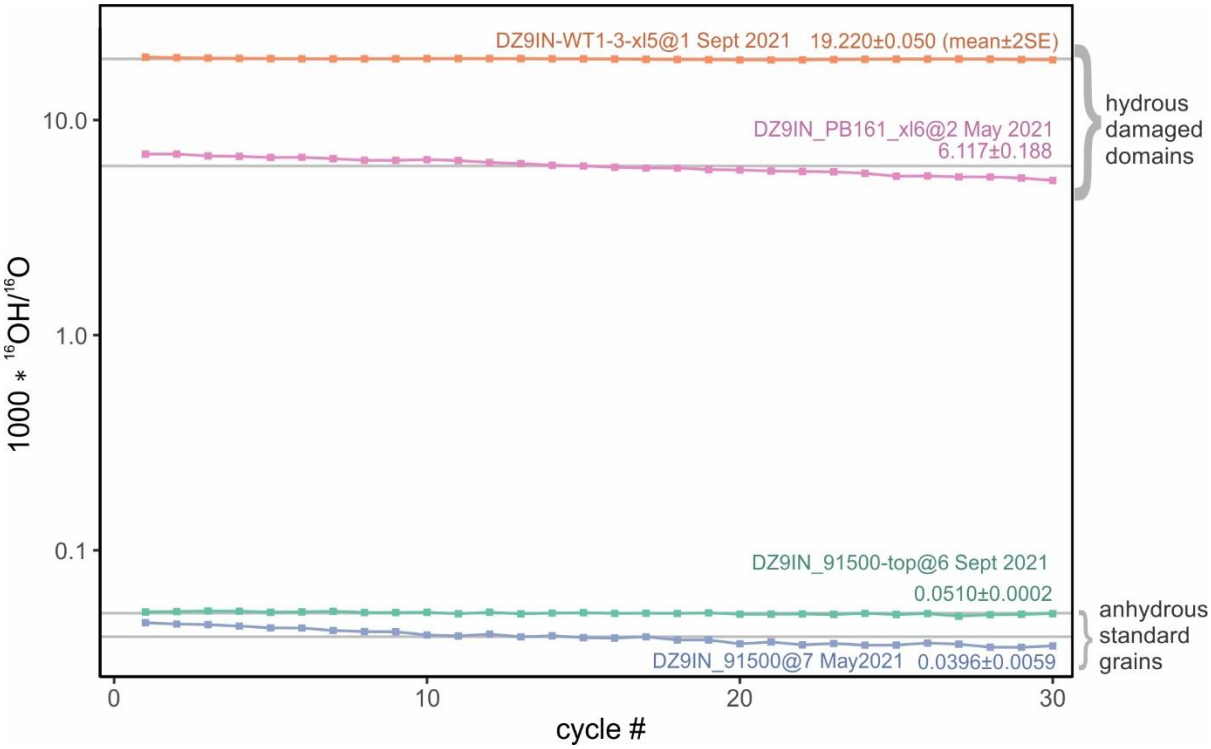

Figure S4. The variability of $^{16}OH/^{16}O$ ratios during individual measurements. Four typical analyses are shown; 2 measurements of 91500 zircon grain (orange) serves as an example of anhydrous measurements. Two measurements of water-containing zircons are shown with yellow and pink colors. The mean and 2 standard errors are indicated. Note that the y-axis is logarithmic.

Chemical abrasion isotope-dilution thermal ionization mass-spectrometry (CA-ID-TIMS)

Zircon grains of PM8 were selected for high-precision measurements by CA-ID-TIMS as this sample displayed highly concordant CL-luminescent zircons with low $\delta^{18}O$ and near-zero $^{16}OH/^{16}O$ signals. The whole grain U-Pb and Pb-Pb analyses were performed at the University of Geneva on a Thermo TRITON equipped with a MasCom discrete dynode electron multiplier. Zircons were annealed at 900°C for 48 hours in quartz crucibles in a muffle furnace. In order to minimize the effects of secondary lead loss each individual zircon grain was placed into pre-cleaned Savillex capsule and chemically abraded in HF + trace HNO_3 at 210°C for 12 hours in Parr bombs (Mattinson, 2005). This caused grains to break up into small pieces, which allowed duplicate measurements of four of the grains using separate fragments of the same original crystal. The grain fragments resulting from the intensive chemical abrasion disintegration of a single zircon crystal were treated separately. This approach allows spatial resolution in the analysed zircon grains. Detailed information about the following dissolution using EARTHTIME ^{202}Pb-^{205}Pb-^{235}U-^{238}U tracer (Condon et al., 2015), chemistry and technical details on instrument calibration, mass fractionation and blank control can be found elsewhere (Awdankiewicz et al., 2021). All common Pb in the zircon analyses was attributed to the procedural blank with the following lead isotopic composition: $^{206}Pb/^{204}Pb = 17.41\pm0.24$, $^{207}Pb/^{204}Pb = 15.31\pm0.15$, $^{208}Pb/^{204}Pb = 36.61\pm0.56$ (1σ). Pb isotope compositions were measured on the electron multiplier, while U (as UO_2) measurements were made either in static Faraday mode using 10^{13}-Ω resistors or on the electron multiplier in case of insufficient signal strength. The accuracy of the measured data was assessed by repeated analysis of the 2 Ga synthetic solution (Condon et al., 2008). The 2 Ga synthetic solution measured with EARTHTIME ^{202}Pb-^{205}Pb-^{235}U-^{238}U tracer yielded mean $^{207}Pb/^{206}Pb = 1999.92\pm0.18/0.37/6.0$ Ma (MSWD=0.86, n=25). All data are reported in the Table S3 with internal errors only, including counting statistics, uncertainties in correcting for mass discrimination, and the uncertainty in the common (blank) Pb composition. Even after

chemical abrasion, $^{206}Pb/^{238}U$ ages showed some scatter and discordance, likely explained by unmitigated Pb loss, so we prefer Th-corrected ^{207}Pb-^{206}Pb ages, which also have less analytical uncertainty.

Triple O isotope measurements

The methodology of O isotope measurements at Georg August University of Göttingen is described in detail previously (Pack et al., 2016). Briefly, mineral separates and whole rock powders were placed in a sample chamber connected to a vacuum line ($P = 10^{-6}$ mbar). The samples were heated with CO_2 laser and reacted with BrF_5 to liberate O_2 gas. The resulted O2 sample was purified by a series of cryogenic traps and subsequently trapped onto molecular sieve. Released from the molecular sieve, the sample O_2 gas was transported through a gas chromatograph via a He carrier gas for further purification of sample from NF-containing compounds. The resulted gas was introduced to a Thermo MAT253 isotope ratio mass spectrometer via dual inlet mode. The uncertainty (obtained from the 1 S.D. external reproducibility of the olivine and garnet standards) is 0.3‰ or better for $\delta^{18}O$ and 0.01‰ for $\Delta^{17}O$.

Definitions: Oxygen isotope notations

In the main text we used the $\delta^{18}O$ notation conventionally defined as $1000\cdot[(^{18}O/^{16}O)_{sample}/(^{18}O/^{16}O)_{VSMOW}-1]$ in ‰, where VSMOW is the Vienna Standard Mean Ocean Water. The $\Delta^{17}O$ notation used for constructing the Figure 3 is expressed as $\Delta^{17}O = \delta^{17}O - 0.528\cdot\delta^{18}O$. Such expression allows for constructing linear arrays through the measurements of hydrothermally altered rocks (see Herwartz et al., 2015)that span a range of W/R, while the meteoric water line and mineral-water fractionation are curved (see Fig. 3). However, following the traditionally accepted notations, the values reported in numbers in

the main text Results section use the linearized $\Delta'^{17}O$ notation, expressed as $10^3\ln(1+\delta^{17}O\cdot10^{-3}) - 0.528\cdot10^3\ln(1+\delta^{18}O\cdot10^{-3})$.

Mineral-mineral and mineral-water fractionation

To construct the linear regression in triple O isotope coordinates we use whole rock values measured directly or calculated from measurements of mineral separates (see **Fig. 3** Main Text). The fractionation between whole rock and mineral separates are estimated empirically from mineral-mineral fractionation and direct measurements. The average fractionation between quartz and whole rock in the studied granitic samples is 0.8 ‰ based on $\delta^{18}O$ measurements. The average fractionation between amphibole and whole rock in granitic samples is -3.1 ‰. Meanwhile, the fractionation between amphibole and whole rock in host rocks -1.3 ‰ (see Fig. S5). These measured fractionations are used to calculate the whole rock $\delta^{18}O$ values from mineral separates. To calculate whole rock $\Delta^{17}O$ values we assume that the fractionation factors are related through the equation $10^3\cdot\ln^{17/16}\alpha_{mineral\text{-}WR} = 0.529\cdot10^3\cdot\ln^{18/16}\alpha_{mineral\text{-}WR}$. The factor 0.529 is derived from assuming high temperature of fractionation (see Herwartz, 2021) given the igneous and metamorphic origin of studied rocks. Since the difference between the $\delta^{18}O$ of co-existing minerals is small (~1-3 ‰), the calculated whole rock $\Delta^{17}O$ value is similar to that of measured minerals. The calculations are carried out used using the linearized notations, e.g., $\delta'^{18}O = 10^3\cdot(1+\delta^{18}O\cdot10^{-3})$, but the conventional δ-notations are used for plotting. The resulted triple O isotope fractionations are depicted in **Fig. S5**. For two samples co-existing mineral pairs are measured, including an aegirine-quartz pair in sample FM20, and a whole rock-amphibole pair in PB172. These measurements yield empirical triple O isotope fractionations with slopes 0.528 and 0.526 in $\delta'^{17}O - \delta'^{18}O$ space, respectively. These are close to the chosen fractionation of 0.529 but slightly lower, which is likely caused by disequilibrium between co-existing minerals.

The calculation of pristine meteoric water is depicted in **Fig. S5**. While the mineral-water fractionations are not calibrated for most mineral species, we show the calibrated quartz-water equilibrium (Sharp et al., 2016) as an example. Since fractionation of oxygen isotopes between quartz and water is amongst the largest in nature (Zheng, 1993), we use the quartz-H_2O equilibrium (Sharp et al., 2016) at temperature of ~600 °C as an approximation for whole rock mineral-water fractionation at a typical hydrothermal temperature of ~300 °C. The water-rock interaction at different W/R would create fluids that are aligned along a trend similar to that outlined by rocks, but with a respective $\delta^{18}O$ – $\Delta^{17}O$ offset caused by fractionation. Fractionation at infinite W/R is accounted for by choosing rock-water fractionation of about 3 ‰.

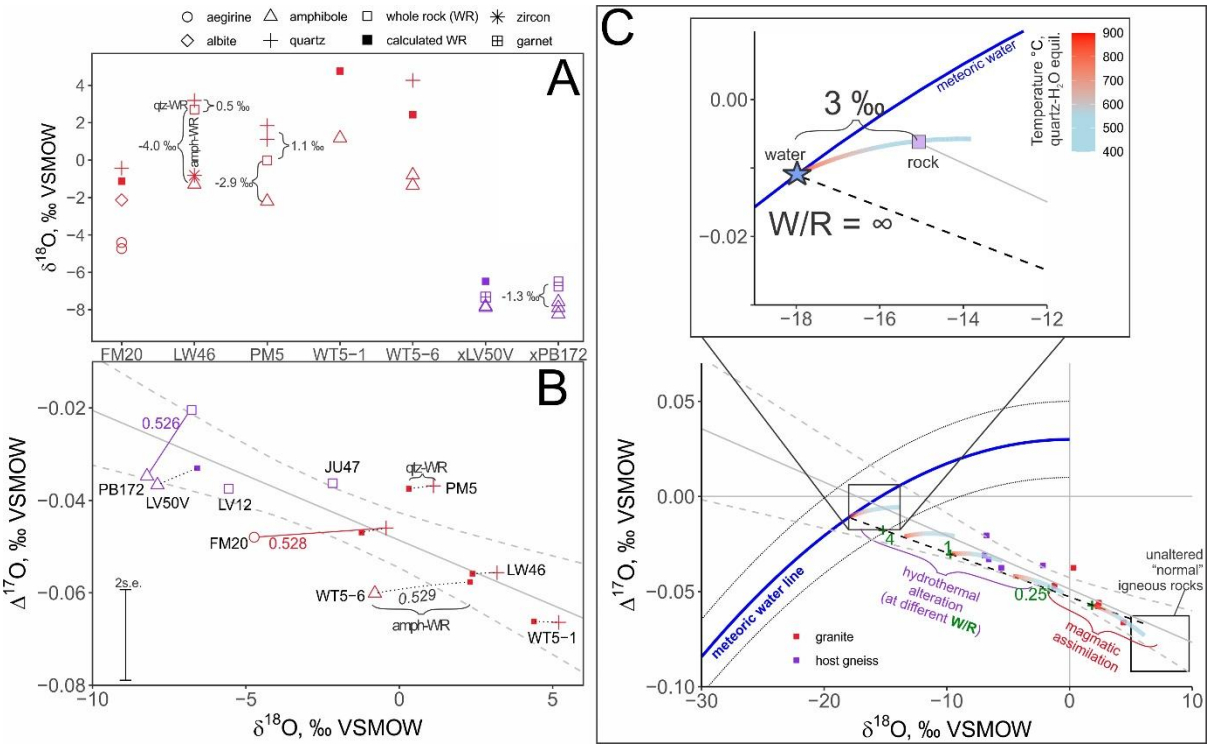

Figure S5. Explanation of how whole rock-mineral and mineral-water triple O isotope fractionations are calculated from mineral separate measurements. **A** – conventional $\delta^{18}O$ measurements of co-existing phases show the consistency of whole rock-mineral fractionations. In these samples, whole rock values (open squares) are ~0.5-1.1 ‰ (0.8 ‰ average) lower than quartz as shown with curly brackets. Whole rock-amphibole fraction is -

3.1 ‰ on average for granitic samples and -1.3 ‰ for the altered host rocks. Using measurements, whole rock values were calculated (filled squared) for the samples, where direct measurements of whole rock powders were not made. **B** – The $\delta^{18}O$ fractionations are used to complement the directly measured whole rock values in the triple O isotope space. To calculate the whole rock $\Delta^{17}O$ values, the triple O isotope exponent (i.e., slope in the $\delta'^{17}O - \delta'^{18}O$ coordinates, commonly denoted as θ) of *0.529* is chosen, as an approximation of mineral-mineral fractionations in high-temperature systems (Pack and Herwartz, 2014). The dotted lines depict such fractionations. Combined, the whole rock dataset is used to draw the linear regression line and the 95% confidence intervals. Solid lines connect measurements of triple oxygen isotope values of co-existing phases, with the numbers representing observed exponents of 0.526 (sample PB172) and 0.528 (FM20). **C** – The diagram showing measured and calculated whole rock values (filled squares) for peralkaline granites and altered host rocks. The regression line is shown along with the array of calculated equilibrium H_2O values (black dashed line) at different water-rock ratios (W/R of 4, 1 and 0.25 are shown in green font). The calculated pristine meteoric water (at W/R of infinity) is shown in the inset. The whole rock-water triple O isotope fractionation is shown with the curly brackets. Roughly, this fractionation is depicted the color-coded curve representing quartz-water equilibrium at different temperatures (Sharp et al., 2016). While the $\delta^{18}O$ fractionation in quartz-water system is substantially larger than for the whole rock-water fractionations, it should follow roughly the same shape. A value of +3 ‰ for $\delta^{18}O$ whole rock-water fractionation is based on assuming that the hydrothermal protolith was composed of equilibrium assemblage of feldspars, quartz, chlorite, amphiboles at 350 °C.

References

Awdankiewicz M., Kryza R., Turniak K., Ovtcharova M. and Schaltegger U. (2021) The Central Sudetic Ophiolite (European Variscan Belt): precise U–Pb zircon dating and geotectonic implications. *Geological Magazine* **158**, 555–566.

Balagansky V. V., Myskova T. A., Lvov P. A., Larionov A. N. and Gorbunov I. A. (2021) Neoarchean A-type acid metavolcanics in the Keivy Terrane, northeastern Fennoscandian Shield: Geochemistry, age, and origin. *Lithos* **380**, 105899.

Batieva I. D. (1976) *Petrology of alkaline granitoids of the Kola Peninsula*., Nauka, St. Petersburg.

Condon D. J., Schoene B., McLean N. M., Bowring S. A. and Parrish R. R. (2015) Metrology and traceability of U–Pb isotope dilution geochronology (EARTHTIME Tracer Calibration Part I). *Geochimica et Cosmochimica Acta* **164**, 464–480.

Condon D., Mclean N., Schoene B., Bowring S., Parrish R. and Noble S. (2008) Synthetic U-Pb 'standard'solutions for ID-TIMS geochronology. *Geochimica et Cosmochimica Acta* **72**, A175–A175.

Herwartz D. (2021) Triple Oxygen Isotope Variations in Earth's Crust. *Reviews in Mineralogy and Geochemistry* **86**, 291–322.

Herwartz D., Pack A., Krylov D., Xiao Y., Muehlenbachs K., Sengupta S. and Di Rocco T. (2015) Revealing the climate of snowball Earth from Δ^{17}O systematics of hydrothermal rocks. *Proc Natl Acad Sci USA* **112**, 5337–5341.

Li X.-H., Long W.-G., Li Q.-L., Liu Y., Zheng Y.-F., Yang Y.-H., Chamberlain K. R., Wan D.-F., Guo C.-H. and Wang X.-C. (2010) Penglai zircon megacrysts: a potential new working reference material for microbeam determination of Hf–O isotopes and U–Pb age. *Geostandards and Geoanalytical Research* **34**, 117–134.

Mattinson J. M. (2005) Zircon U–Pb chemical abrasion ("CA-TIMS") method: combined annealing and multi-step partial dissolution analysis for improved precision and accuracy of zircon ages. *Chemical Geology* **220**, 47–66.

Pack A. and Herwartz D. (2014) The triple oxygen isotope composition of the Earth mantle and understanding ΔO17 variations in terrestrial rocks and minerals. *Earth and Planetary Science Letters* **390**, 138–145.

Pack A., Tanaka R., Hering M., Sengupta S., Peters S. and Nakamura E. (2016) The oxygen isotope composition of San Carlos olivine on the VSMOW2-SLAP2 scale: San Carlos olivine on the VSMOW2-SLAP2 scale. *Rapid Commun. Mass Spectrom.* **30**, 1495–1504.

Sharp Z. D., Gibbons J. A., Maltsev O., Atudorei V., Pack A., Sengupta S., Shock E. L. and Knauth P. L. (2016) A calibration of the triple oxygen isotope fractionation in the SiO2–H2O system and applications to natural samples. *Geochimica et Cosmochimica Acta* **186**, 105–119.

Wiedenbeck M., Hanchar J. M., Peck W. H., Sylvester P., Valley J., Whitehouse M., Kronz A., Morishita Y., Nasdala L. and Fiebig J. (2004) Further characterisation of the 91500 zircon crystal. *Geostandards and Geoanalytical Research* **28**, 9–39.

Zheng Y.-F. (1993) Calculation of oxygen isotope fractionation in anhydrous silicate minerals. *Geochimica et Cosmochimica Acta* **57**, 1079–1091.